

The Event-Camera Dataset: Event-based Data for Pose Estimation, Visual Odometry, and SLAM

Elias Mueggler¹, Henri Rebecq¹, Guillermo Gallego¹, Tobi Delbrück² and Davide Scaramuzza¹

Abstract

New vision sensors, such as the Dynamic and Active-pixel Vision sensor (DAVIS), incorporate a conventional global-shutter camera and an event-based sensor in the same pixel array. These sensors have great potential for high-speed robotics and computer vision because they allow us to combine the benefits of conventional cameras with those of event-based sensors: low latency, high temporal resolution, and very high dynamic range. However, new algorithms are required to exploit the sensor characteristics and cope with its unconventional output, which consists of a stream of asynchronous brightness changes (called events) and synchronous grayscale frames. For this purpose, we present and release a collection of datasets captured with a DAVIS in a variety of synthetic and real environments, which we hope will motivate research on new algorithms for high-speed and high-dynamic-range robotics and computer-vision applications. In addition to global-shutter intensity images and asynchronous events, we also provide inertial measurements and ground truth from a motion-capture system. All the data are released both as standard text files and binary files (i.e., rosbag). This paper provides an overview of the available data.

Keywords

Event-based cameras, visual odometry, SLAM

Dataset Website

All datasets can be found on the web:

http://rpg.ifi.uzh.ch/davis_data.html

A video containing visualizations of the datasets:

<https://youtu.be/bVVBTQ7136I>

Introduction

Over the past fifty years, computer-vision research has been devoted to standard, frame-based cameras (i.e., rolling or global shutter cameras) and only in the last few years cameras have been successfully used in commercial autonomous mobile robots, such as cars, drones, and vacuum cleaners, just to mention a few. Despite the recent progress, we believe that the advent of event-based cameras is about to revolutionize the robot sensing landscape. Indeed, the performance of a mobile robot in tasks, such as navigation, depends on the accuracy and latency of perception. The latency depends on the frequency of the sensor data plus the time it takes to process the data. It is typical in current robot-sensing pipelines to have latencies in the order of 50-200ms or more, which puts a hard bound on the maximum agility of the platform. An event-based camera virtually eliminates the latency: data is transmitted using events, which have a latency in the order of microseconds. Another advantage of event-based cameras is their very high dynamic range (130 dB vs. 60 dB of standard cameras), which makes them ideal in scenes characterized by large illumination changes. Other key properties of event-based cameras are low-bandwidth, low-storage, and low-power requirements. All these properties enable the design of a new class of

algorithms for high-speed and high-dynamic-range robotics, where standard cameras are typically not ideal because of motion blur, image saturation, and high latency. However, the way that event-based cameras convey the information is completely different from that of traditional sensors, so that a new paradigm shift is needed to deal with them.

Related Datasets

There exist two recent datasets that also use the DAVIS: (Rueckauer and Delbrück 2016) and (Barranco et al. 2016).

The first work is tailored for comparison of event-based optical flow estimation algorithms (Rueckauer and Delbrück 2016). It contains both synthetic and real datasets under pure rotational (3-DOF) motion on simple scenes with strong visual contrasts. Ground truth was acquired using the inertial measurement unit (IMU). In contrast, our datasets contain arbitrary, hand-held, 6-DOF motion in a variety of artificial and natural scenes with precise ground truth from a motion-capture system.

A more similar work to ours is (Barranco et al. 2016). Their focus is to create a dataset that facilitates comparison

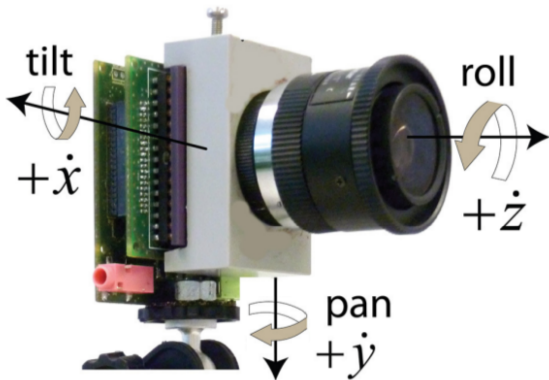
¹Robotics and Perception Group, University of Zurich, Switzerland

²Institute of Neuroinformatics, University of Zurich and ETH Zurich, Switzerland

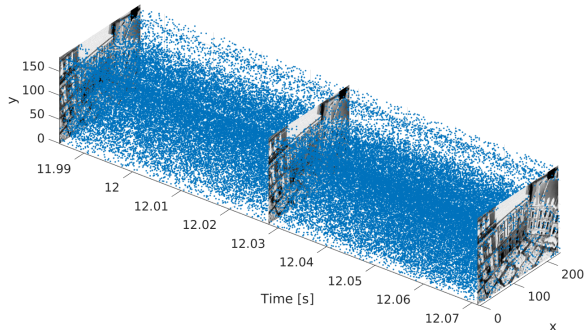
Corresponding author:

Elias Mueggler, Robotics and Perception Group, University of Zurich, Switzerland. E-mail: mueggler@ifi.uzh.ch

This work was supported by the DARPA FLA Program, the Google Faculty Research Award, the Qualcomm Innovation Fellowship, the National Centre of Competence in Research Robotics (NCCR), the Swiss National Science Foundation, and the UZH Forschungskredit.



(a) The DAVIS sensor and axes definitions. Figure adapted from (Delbrück et al. 2014)



(b) Visualization of the event output of a DAVIS in space-time. Colored dots mark individual asynchronous events. The polarity of the events is not shown.

Figure 1. The DAVIS camera and visualization of its output.

of event-based and frame-based methods for 2D and 3D visual navigation tasks. To this end, a ground robot was equipped with a DAVIS and a Microsoft Kinect RGB-D sensor. The DAVIS was mounted on a pan-tilt unit, thus it could be excited in five degrees of freedom. The scene contains checkerboards, books, and a chair. Ground truth was acquired by the encoders of pan-tilt unit and the ground robot's wheel odometry, and is therefore subject to drift. In contrast, our dataset contains hand-held, 6-DOF motion (slow- and high-speed) on a variety of scenes with precise ground truth from a motion-capture system, which is not subject to drift.

The DAVIS Sensor

The Dynamic and Active-pixel Vision Sensor (DAVIS) (Brandli et al. 2014) (see Fig. 1a) is an event camera that transmits *events* in addition to frames. Events are pixel-level, relative-brightness changes that are detected in continuous time by specially-designed pixels*. The events are timestamped with *micro-second* resolution and transmitted asynchronously at the time they occur. Each event e is a tuple $\langle x, y, t, p \rangle$, where x, y are the pixel coordinates of the event, t is the timestamp of the event, and $p = \pm 1$ is the polarity of the event, which is the sign of the brightness change. This representation is sometimes also referred to as Address-Event Representation (AER). The DAVIS has a spatial resolution of 240×180 pixels. A visualization of the event output is shown in Fig. 1b. Both

the events and frames are generated by the same physical pixels, hence there is no spatial offset between the events and the frames.

Due to its low latency and high temporal resolution, both in the range of *micro-seconds*, event-based cameras are very promising sensors for high-speed mobile robot applications. Since event cameras are data-driven (only brightness *changes* are transmitted), no redundant data is transmitted. The required bandwidth thus depends on the motion speed and the type of scene. An additional advantage for robotic applications is the high dynamic range of 130 dB (compared to 60 dB of expensive computer-vision cameras), which allows both indoor and outdoor operation without changing parameters. Since all pixels are independent, very large contrast changes can also take place within the same scene.

Over the course of the last seven years, we and other groups have demonstrated the use of event-based sensors in a variety of tasks, such as SLAM in 2D (Weikersdorfer et al. 2013) and 3D (Kim et al. 2016), optical flow (Cook et al. 2011; Benosman et al. 2014; Bardow et al. 2016), visual odometry (Censi and Scaramuzza 2014), 6-DoF localization for high-speed robotics (Mueggler et al. 2014), mosaicing (Kim et al. 2014), and continuous-time trajectory estimation (Mueggler et al. 2015).

However, all these methods were evaluated on different, specific datasets and, therefore, cannot be compared against each other. The datasets we propose here are tailored to allow comparison of pose tracking, visual odometry, and SLAM algorithms. Since event-based cameras, such as the DAVIS, are currently still expensive (5,000 USD), these data also allows researchers without equipment to use well-calibrated data for their research.

DAVIS IMU

In addition to the visual output (events and frames), the DAVIS includes an IMU that provides gyro and accelerometer data, thus enabling to design visual-inertial event-based algorithms. The DAVIS cameras has the IMU mounted directly behind and centered under the image sensor pixel array center, at a distance of about 3 mm from it, so that the IMU shares nearly the same position as the event sensor. The IMU axes are aligned with the camera axes (see Fig. 1a). More specifically, the IMU is an InvenSense MPU-6150[†], which integrates a three-axis gyroscope that can measure in the range $\pm 2,000^\circ/\text{s}$ and a three-axis accelerometer for the range $\pm 16g$. It integrates six 16-bit ADCs for digitizing the gyroscope and accelerometer outputs at 1 kHz sample rate.

DAVIS Simulator

Simulation offers a good baseline when working with new sensors, such as the DAVIS. Based on the operation principle of an ideal DAVIS pixel, we created a simulator that, given a virtual 3D scene and the trajectory of a moving DAVIS within it, generates the corresponding stream of events and intensity frames. We used the computer graphics software

* Video illustration: <https://youtu.be/LauQ6LWTkxM>

[†] IMU data sheet: <https://store.invensense.com/ProductDetail/MPU6150-invensense/470090/>

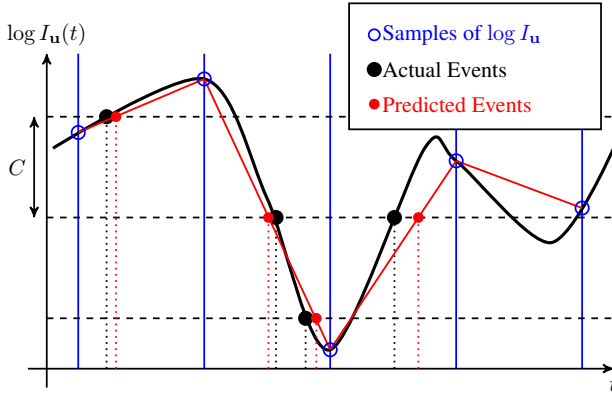


Figure 2. DAVIS Simulator. Per-pixel event generation using piecewise linear time interpolation of the intensities given by the rendered images. For simplicity, images were rendered at a fixed rate.

Blender[‡] to generate thousands of rendered images along the specified trajectory, ensuring that the motion between consecutive images was smaller than 1/3 pixel. For each pixel, we keep track of the time of the last event triggered at that location. This map of timestamps (also called surface of active events (Benosman et al. 2014)), combined with time interpolation of the rendered image intensities, allows determining brightness changes of predefined amount (given by the contrast threshold) in the time between images, thus effectively providing continuous timestamps, as if events were generated asynchronously. Time interpolation has an additional benefit: it solves the problem of having to generate millions of images per second of sequence, as it would have been required to deliver microsecond-resolution timestamps in the absence of interpolation.

More specifically, Fig. 2 illustrates the operation of the simulator for a single pixel $\mathbf{u} = (x, y)^\top$. The continuous intensity signal at pixel \mathbf{u} , $\log I_{\mathbf{u}}(t)$ (black) is sampled at the times of the rendered images (blue markers). These samples are used to determine the times of the events: the data is linearly interpolated between consecutive samples and the crossings of the resulting lines (in red) with the levels given by multiples of the contrast threshold C (i.e., horizontal lines) specify the timestamps of the events (red dots). As it can be observed, this simple interpolation scheme allows for (i) higher resolution event time stamps than those of the rendered images, and (ii) the generation of multiple events between two samples if the corresponding intensity jump is larger than the contrast threshold.

The provided events are “perfect” measurements up to sampling and quantization; under this condition, an image $\hat{I}(\mathbf{u}; t)$ can be reconstructed from the event stream at any point in time t by accumulating events $e_k = \langle \mathbf{u}_k, t_k, p_k \rangle$ according to

$$\log \hat{I}(\mathbf{u}; t) = \log I(\mathbf{u}; 0) + \sum_{0 < t_k \leq t} p_k C \delta(\mathbf{u} - \mathbf{u}_k),$$

where $I(\mathbf{u}; 0)$ is the rendered image at time $t = 0$ and δ selects the pixel to be updated on every event. We used this scheme to check that the reconstructed image agreed with the rendered image at several points in time; specifically, the per-pixel intensity error was confined to the quantization interval $(-C, C)$.

Event generation operates on brightness pixels, which are computed from the rendered color images using the ITU-R Recommendation BT.601[§] for luma, i.e., according to formula $Y = 0.299R + 0.587G + 0.114B$, with RGB channels in linear color space to better resemble the operation of the DAVIS.

Because realistic event noise is extremely difficult to model due to the complex behavior of event sensors with respect to their bias settings and other factors, the provided simulation datasets do not include event noise. Nevertheless, these datasets are a useful tool for prototyping new event-based algorithms.

Datasets

In this section, we describe the datasets that we provide. The datasets contain:

- the event stream,
- intensity images at about 24 Hz,
- inertial measurements (3-axis gyroscope and 3-axis accelerometer) at 1 kHz,
- ground truth from a motion-capture system[¶] with sub-millimeter precision at 200 Hz (for the indoor datasets),
- the intrinsic camera matrix.

For datasets that were captured outside the motion-capture system (e.g., in an office or outdoors), no ground truth is provided. Some datasets were collected using a motorized linear slider and ground truth was collected using the slider’s position. Due to vibrations induced by the slider motor, the very noisy IMU data was not recorded.

Data Format

The datasets are provided in standard text form that is described here. For convenience, they can also be downloaded as binary rosbag files (the details are on the website). The format of the text files is described in Table 1.

The ground truth pose is with respect to the (arbitrary) motion-capture origin that has the z-axis gravity-aligned (pointing upwards). The orientation is provided as a unit quaternion $\mathbf{q} = (q_x, q_y, q_z, q_w)^\top$, where q_w and $\mathbf{q}_v = (q_x, q_y, q_z)^\top$ are the scalar and vector components, respectively. This convention was proposed as a standard by JPL (Breckenridge 1979).

All values are reported in SI units. While the timestamps were originally recorded as POSIX, we subtracted the lowest timestamp as offset such that all datasets start at zero. This helps to avoid numerical difficulties when dealing with microsecond resolution timestamps of the events.

Images are provided as PNG files. The list of all images and their timestamps is provided in a separate file. The typical framerate is 24 Hz, but it varies with the exposure time.

The IMU axes are aligned with the optical coordinate frame (i.e., the positive z-axis is identical to the optical axis and so are the x and y-axes).

[‡]<https://www.blender.org/>

[§]<https://www.itu.int/rec/R-REC-BT.601>

[¶]We use an OptiTrack system from NaturalPoint.

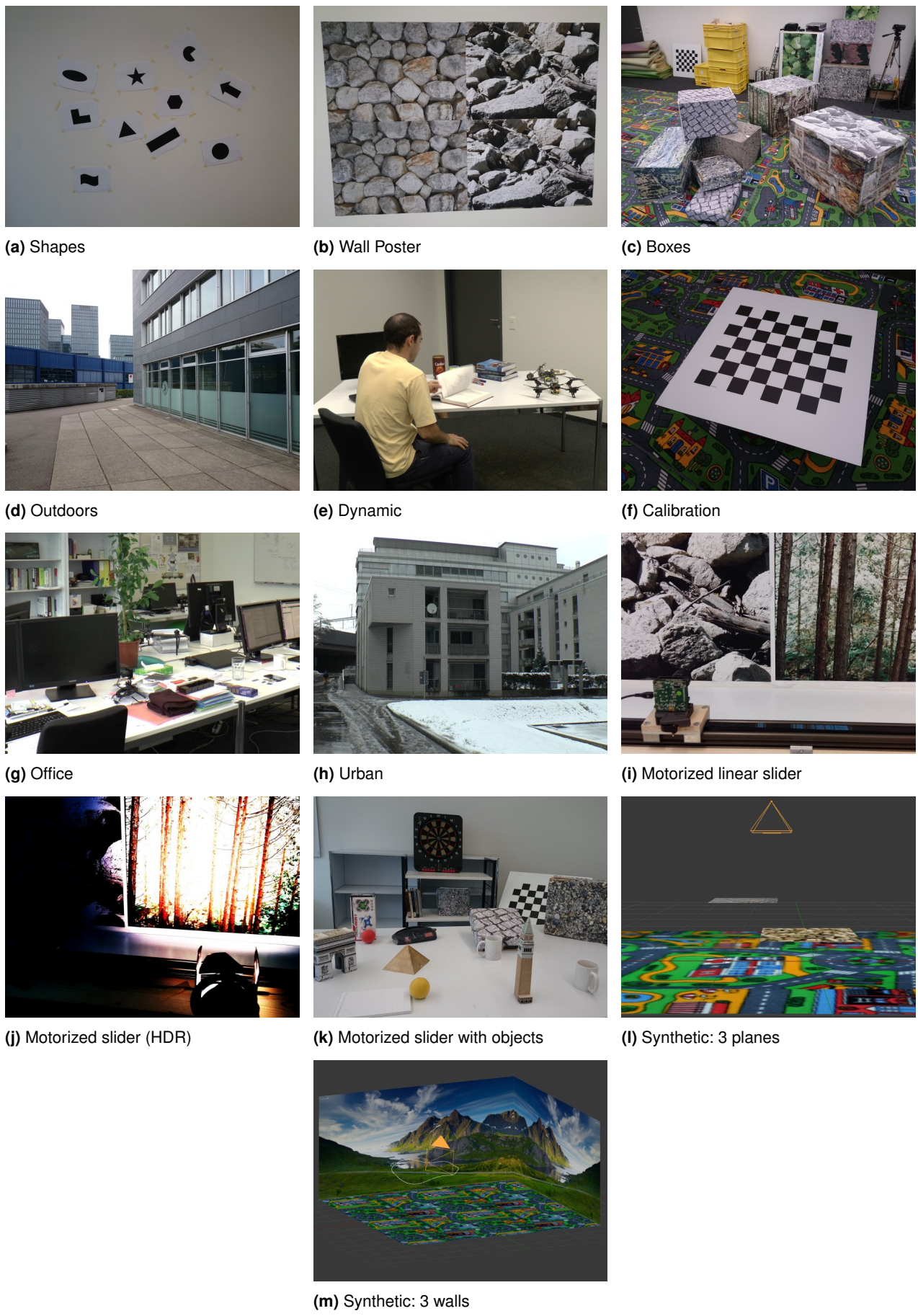


Figure 3. Dataset scenes

File	Description	Line Content
events.txt	One event per line	timestamp x y polarity
images.txt	One image reference per line	timestamp filename
images/00000000.png	Images referenced from images.txt	
imu.txt	One measurement per line	timestamp ax ay az gx gy gz
groundtruth.txt	One ground truth measurements per line	timestamp px py pz qx qy qz qw
calib.txt	Camera parameters	fx fy cx cy d0 d1 d2 d3 d4

Table 1. Description of Dataset Format

List of Datasets

The provided datasets are summarized in Table 2 and Fig. 3. All the datasets contain increasing speeds, different scenes, and varying degrees of freedom:^{||}. for the shapes, poster, and boxes datasets, the motion first starts with excitation of each single degree of freedom separately; then combined and faster excitations are performed. This leads to increasing difficulty and a higher event rate over time.

In the high dynamic range (HDR) sequences (hdr_poster, hdr_boxes, and slider_hdr), a spotlight was used to create large intrascene contrasts. For hdr_poster, we measured 80lx and 2,400lx in the dark and bright areas, respectively.

The outdoors datasets were acquired in an urban environment both walking and running. While no ground truth is available, we returned precisely to the same location after a large loop.

The dynamic datasets were collected in a mock-up office environment viewed by the motion-capture system, with a moving person first sitting at a desk, then moving around.

A calibration dataset is also available, for instance in case the user wishes to use a different camera model or different methods for hand-eye calibration. The dimensions of the calibration pattern (a checkerboard) are 6×9 tiles of 40 mm. For the lower half of the table, different settings (lenses, focus, etc.) were used. Thus, while we provide the intrinsic calibration, no calibration datasets are available.

The slider_close, slider_far, slider_hdr_close, and slider_hdr_far datasets were recorded with a motorized linear slider parallel to a textured wall at 23.1 cm, 58.4 cm, 23.2 cm, and 58.4 cm, respectively.

For the datasets, we applied two different sets of biases (parameters) for the DAVIS as listed in Table 3. The first set, labeled “indoors”, was used in all datasets but outdoors_walking, outdoors_running, and urban, where the set “outdoors” was applied. For the simulated datasets, we used a contrast threshold of $\pm 15\%$ and $\pm 20\%$ for the simulation_3planes and simulation_3walls, respectively.

Calibration

First, we calibrated the DAVIS intrinsically using a checkerboard pattern. Then, we computed the hand-eye calibration that we applied to the subsequent dataset recordings so that the ground truth poses that we provide are those of the event camera (i.e., the “eye”), not those of the motion-capture trackable (i.e., the “hand”) attached to the camera. We also included a calibration dataset in case

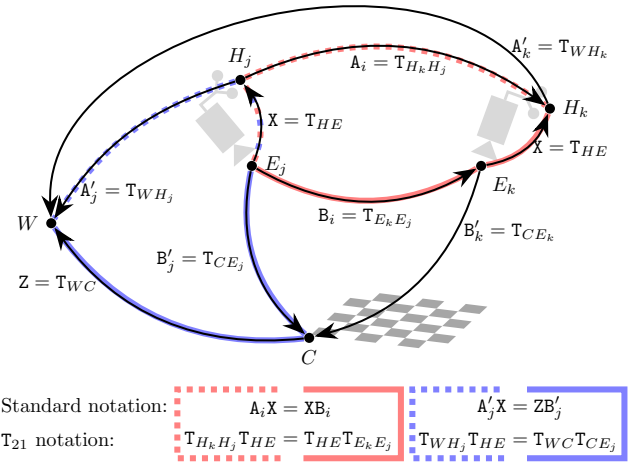


Figure 4. Hand-eye calibration. Coordinate frames and transformations involved in case of the hand-eye device at two different positions (j and k). The red loop between two stations of the hand-eye device is used in the first type of hand-eye calibration problems, of the form $A_i X = X B_i$, and the blue loop is used in the second type of hand-eye calibration problems, of the form $A'_j X = Z B'_j$. We use a combination of both approaches to solve for the constant, hand-eye calibration transform X .

a different camera model or improved hand-eye calibration method is required.

Intrinsic Camera Calibration

We used the standard pinhole camera model with radial-tangential distortion using the implementation of ROS and OpenCV**. We used three radial distortion coefficients (k_1 , k_2 , and $k_3 = 0$) and two for tangential distortion (p_1 and p_2). We provide a dataset for post-calibration in case that another method is preferred.

Hand-Eye Calibration

For the indoor datasets, we provide accurate and high-frequency (200 Hz) pose data from a motion-capture system. However, the coordinate frame used by the motion-capture system is different from the optical coordinate frame of the DAVIS. Thus, we performed a hand-eye calibration before capturing the datasets. Fig. 4 shows the coordinate frames and transformations used to solve the hand-eye calibration problem. The frames are those of the world W , the hand H , the camera E (Fig. 1a), and the checkerboard

^{||}The DAVIS was moved by hand, the dominant motion is described.

**http://wiki.ros.org/camera_calibration/Tutorials/MonocularCalibration

Name	Motion	Scene	GT	T [s]	TS [m/s]	RS [°/s]	NE [-]
shapes_rotation	Rotation, incr. speed	Fig. 3a	yes	59.8	0.83	730	23,126,288
shapes_translation	Translation, incr. speed	Fig. 3a	yes	59.7	2.60	271	17,363,976
shapes_6dof	6 DOF, incr. speed	Fig. 3a	yes	59.7	2.35	715	17,962,477
poster_rotation	Rotation, incr. speed	Fig. 3b	yes	59.8	0.84	884	169,350,136
poster_translation	Translation, incr. speed	Fig. 3b	yes	59.8	2.58	240	100,033,286
poster_6dof	6 DOF, incr. speed	Fig. 3b	yes	59.8	2.51	937	133,464,530
boxes_rotation	Rotation, incr. speed	Fig. 3c	yes	59.8	0.85	669	185,688,947
boxes_translation	Translation, incr. speed	Fig. 3c	yes	59.8	3.43	319	112,388,307
boxes_6dof	6 DOF, incr. speed	Fig. 3c	yes	59.8	3.84	509	133,085,511
hdr_poster	6 DOF, incr. speed	Fig. 3b	yes	59.8	2.28	597	102,910,720
hdr_boxes	6 DOF, incr. speed	Fig. 3c	yes	59.8	2.94	592	118,499,744
outdoors_walking	6 DOF, walking	Fig. 3d	no [†]	133.4	n/a	n/a	64,517,638
outdoors_running	6 DOF, running	Fig. 3d	no [†]	87.6	n/a	n/a	98,572,164
dynamic_rotation	Rotation, incr. speed	Fig. 3e	yes	59.8	0.45	542	71,324,510
dynamic_translation	Translation, incr. speed	Fig. 3e	yes	59.8	1.86	227	35,809,924
dynamic_6dof	6 DOF, incr. speed	Fig. 3e	yes	59.7	2.91	627	57,174,637
calibration	6 DOF, slow	Fig. 3f	yes	59.8	0.32	67	21,340,629
office_zigzag	6-DOF, zigzag, slow	Fig. 3g	no	10.9	n/a	n/a	7,735,308
office_spiral	6-DOF, spiral, slow	Fig. 3g	no	11.2	n/a	n/a	6,254,774
urban	Linear, slow	Fig. 3h	no	10.7	n/a	n/a	5,359,539
slider_close	Linear, const. speed	Fig. 3i	yes [*]	6.5	0.16	0	4,032,668
slider_far	Linear, const. speed	Fig. 3i	yes [*]	6.4	0.16	0	3,442,683
slider_hdr_close	Linear, const. speed	Fig. 3j	yes [*]	6.5	0.16	0	3,337,787
slider_hdr_far	Linear, const. speed	Fig. 3j	yes [*]	6.5	0.16	0	2,509,582
slider_depth	Linear, const. speed	Fig. 3k	yes [*]	3.4	0.32	0	1,078,541
simulation_3planes	Translation, circle	Fig. 3l	yes [#]	2.0	0.63	0	1,332,223
simulation_3walls	6 DOF	Fig. 3m	yes [#]	2.0	5.31	109	4,104,833

Table 2. List of Datasets. Note that the calibration dataset only applies to the upper half of the table. The other datasets use different lenses and calibrations. GT: Ground truth. T: Duration. TS: Maximum translation speed. RS: Maximum rotational speed. NE: Number of events. [†]Same start and end pose after a large loop. ^{*}Ground truth from motorized linear slider. No IMU data due to vibrations. [#]Simulated DAVIS using Blender. No IMU data included.

Bias	Indoors		Outdoors	
	Coarse	Fine	Coarse	Fine
DiffBn	2	39	4	39
OFFBn	1	62	4	0
ONBn	4	200	6	200
PrBp	3	72	2	58
PrSFBp	3	96	1	33
RefrBp	3	52	4	25

Table 3. List of biases applied to the DAVIS. The DAVIS uses two stages of biases, coarse and fine, which are both listed here.

C. For the transformations, Fig. 4 shows both the compact standard notation of hand-eye calibration problems and a more explicit one: the Euclidean transformation T_{21} (4×4 homogeneous matrix representation) maps points from frame 1 to frame 2 according to $\mathbf{P}_2 = T_{21}\mathbf{P}_1$.

More specifically, we first use a linear algorithm (Tsai and Lenz 1989) to provide an initial solution of the hand-eye calibration problem $\{\mathbf{A}_i\mathbf{X} = \mathbf{X}\mathbf{B}_i\}_{i=1}^N$, where $\mathbf{A}_i \leftrightarrow \mathbf{B}_i$ are N correspondences of relative hand-hand ($\mathbf{A}_i := \mathbf{T}_{H_k H_j}$) and eye-eye ($\mathbf{B}_i := \mathbf{T}_{E_k E_j}$) poses at different times (j and k), respectively, and $\mathbf{X} := \mathbf{T}_{HE}$ is the unknown eye-to-hand transformation. Then, using the second formulation of hand-eye calibration problems, of the form $\{\mathbf{A}'_j\mathbf{X} = \mathbf{Z}\mathbf{B}'_j\}_{j=1}^N$,

where $\mathbf{A}'_j := \mathbf{T}_{WH_j}$ and $\mathbf{B}'_j := \mathbf{T}_{CE_j}$ are the hand-to-motion-capture and eye-to-checkerboard transformations for the j -th pose, respectively, we refined \mathbf{T}_{HE} by jointly estimating the hand-eye \mathbf{X} and robot-world $\mathbf{Z} := \mathbf{T}_{WC}$ (i.e., motion-capture–checkerboard) transformations that minimize the reprojection error in the image plane:

$$\min_{\mathbf{X}, \mathbf{Z}} \sum_{mn} d^2(\mathbf{x}_{mn}, \hat{\mathbf{x}}_{mn}(\mathbf{X}, \mathbf{Z}; \mathbf{A}'_m, \mathbf{P}_n, \mathbf{K})),$$

where $d^2(\mathbf{x}_{mn}, \hat{\mathbf{x}}_{mn})$ is the squared Euclidean distance between the measured projection \mathbf{x}_{mn} of the n -th checkerboard corner \mathbf{P}_n on the m -th camera and the predicted corner $\hat{\mathbf{x}}_{mn} = \mathbf{f}(\hat{\mathbf{B}}'_m; \mathbf{P}_n, \mathbf{K})$, which is a function of the intrinsic camera parameters \mathbf{K} and the extrinsic parameters $\hat{\mathbf{B}}'_m := \mathbf{Z}^{-1}\mathbf{A}'_m\mathbf{X}$ predicted using the motion-capture data. This non-linear least-squares problem is solved iteratively using the Gauss-Newton method. The initial value of \mathbf{Z} is given by $\mathbf{Z} = \mathbf{A}'_1\mathbf{X}\mathbf{B}'_1^{-1}$, with \mathbf{X} provided by the linear algorithm. We included a dataset for post-calibration in case another method is preferred.

The ground-truth pose gives the position and orientation of the event camera with respect to the world (i.e., the motion-capture system). Hence, it already incorporates the computed hand-eye transformation. That is, while the motion-capture system outputs \mathbf{T}_{WH_j} , we apply the hand-eye calibration $\mathbf{T}_{HE} \equiv \mathbf{T}_{HE_j} \forall j$ and directly report $\mathbf{T}_{WE_j} = \mathbf{T}_{WH_j}\mathbf{T}_{HE_j}$ as ground truth pose.

Known Issues

Clock Drift and Offset

The clocks from motion-capture system and the DAVIS are not hardware synchronized. We observed clock drift of about 2 ms/min. To counteract the clock drift, we reset the clocks before each dataset recording. Since all datasets are rather short (in the order of 1 min), the effect of drift is negligible. A small, dataset-dependent offset between the DAVIS and motion-capture timestamps is present since the timestamps were reset in software.

References

Bardow P, Davison AJ and Leutenegger S (2016) Simultaneous optical flow and intensity estimation from an event camera. In: *IEEE Int. Conf. Computer Vision and Pattern Recognition (CVPR)*.

Barranco F, Fermuller C, Aloimonos Y and Delbruck T (2016) A dataset for visual navigation with neuromorphic methods. *Frontiers in Neuroscience* 10(49).

Benosman R, Clercq C, Lagorce X, Ieng SH and Bartolozzi C (2014) Event-based visual flow. *IEEE Trans. Neural Netw. Learn. Syst.* 25(2): 407–417.

Brandli C, Berner R, Yang M, Liu SC and Delbruck T (2014) A 240x180 130dB 3us latency global shutter spatiotemporal vision sensor. *IEEE J. of Solid-State Circuits* 49(10): 2333–2341. DOI:10.1109/JSSC.2014.2342715.

Breckenridge WG (1979) Quaternions proposed standard conventions. Technical report, NASA Jet Propulsion Laboratory.

Censi A and Scaramuzza D (2014) Low-latency event-based visual odometry. In: *IEEE Int. Conf. on Robotics and Automation (ICRA)*.

Cook M, Gugelmann L, Jug F, Krautz C and Steger A (2011) Interacting maps for fast visual interpretation. In: *Int. Joint Conf. on Neural Networks (IJCNN)*. pp. 770–776.

Delbruck T, Villanueva V and Longinotti L (2014) Integration of dynamic vision sensor with inertial measurement unit for electronically stabilized event-based vision. In: *Int. Conf. on Circuits and Systems (ISCAS)*. pp. 2636–2639.

Kim H, Handa A, Benosman R, Ieng SH and Davison AJ (2014) Simultaneous mosaicing and tracking with an event camera. In: *British Machine Vision Conf. (BMVC)*.

Kim H, Leutenegger S and Davison A (2016) Real-time 3D reconstruction and 6-DoF tracking with an event camera. In: *Eur. Conf. on Computer Vision (ECCV)*.

Mueggler E, Gallego G and Scaramuzza D (2015) Continuous-time trajectory estimation for event-based vision sensors. In: *Robotics: Science and Systems (RSS)*.

Mueggler E, Huber B and Scaramuzza D (2014) Event-based, 6-DOF pose tracking for high-speed maneuvers. In: *IEEE/RSJ Int. Conf. on Intelligent Robots and Systems (IROS)*.

Rueckauer B and Delbruck T (2016) Evaluation of event-based algorithms for optical flow with ground-truth from inertial measurement sensor. *Frontiers in Neuroscience* 10(176).

Tsai RY and Lenz RK (1989) A New Technique for Fully Autonomous and Efficient 3D Robotics Hand/Eye Calibration. *IEEE Trans. Robotics* 5(3): 345–358.

Weikersdorfer D, Hoffmann R and Conradt J (2013) Simultaneous localization and mapping for event-based vision systems. In: *Int. Conf. on Computer Vision Systems (ICVS)*.